

# Conditional Training with Bounding Map for Universal Lesion Detection

Han Li<sup>1,2</sup>, Long Chen<sup>2,3</sup>, Hu Han<sup>2✉</sup>, and S. Kevin Zhou<sup>2✉</sup>

School of AI, University of the Chinese Academy of Science  
 Medical Imaging, Robotics, Analytic Computing Laboratory/Engineering  
 (MIRACLE), Key Laboratory of Intelligent Information Processing of Chinese  
 Academy of Sciences (CAS), Institute of Computing Technology, CAS, Beijing, China  
 School of Electronic, Electrical and Communication Engineering, University of the  
 Chinese Academy of Science  
 {han.li,long.chen}@miracle.ict.ac.cn, {hanhu,zhoushaohua}@ict.ac.cn

**Abstract.** Universal Lesion Detection (ULD) in computed tomography plays an essential role in computer-aided diagnosis. Promising ULD results have been reported by coarse-to-fine two-stage detection approaches, but such two-stage ULD methods still suffer from issues like imbalance of positive v.s. negative anchors during object proposal and insufficient supervision problem during localization regression and classification of the region of interest (RoI) proposals. While leveraging pseudo segmentation masks such as bounding map (BM) can reduce the above issues to some degree, it is still an open problem to effectively handle the diverse lesion shapes and sizes in ULD. In this paper we propose a BM-based conditional training for two-stage ULD, which can (i) reduce positive vs. negative anchor imbalance via a BM-based conditioning (BMC) mechanism for anchor sampling instead of traditional IoU-based rule; and (ii) adaptively compute size-adaptive BM (ABM) from lesion bounding-box, which is used for improving lesion localization accuracy via ABM-supervised segmentation. Experiments with four state-of-the-art methods show that the proposed approach can bring an almost free detection accuracy improvement without requiring expensive lesion mask annotations.

**Keywords:** Universal lesion detection · Adaptive bounding map · Conditional training.

## 1 Introduction

Universal Lesion Detection (ULD) in computed tomography (CT) [1–13], which aims to localize different types of lesions instead of identifying lesion types [14–25], plays an essential role in computer-aided diagnosis (CAD). ULD is a challenging task because different lesions have very diverse shapes and sizes, easily leading to false positive and false negative detections. Most existing ULD methods are mainly inspired by the successful deep models in object detection

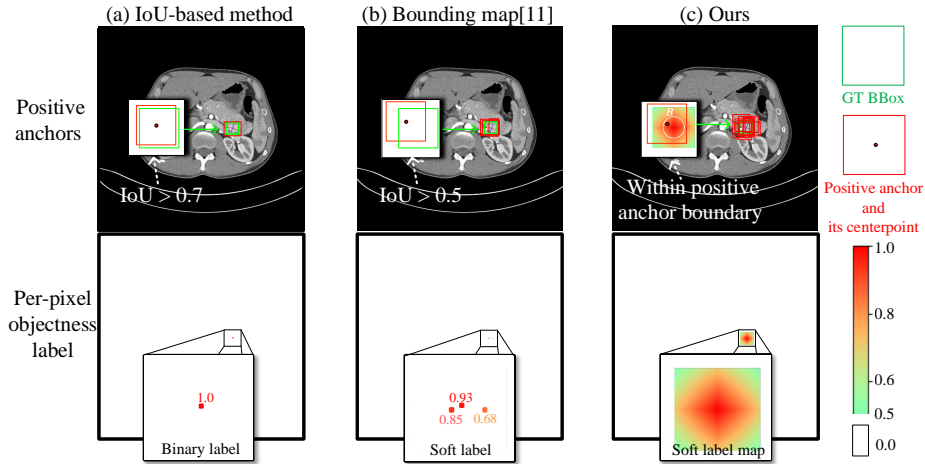


**Fig. 1.** The IoU-based method (a) produces very few positive anchors thus biases the RPN training. The BM method [11] (b) relieves this issue to some degree via a soft-label map BM and a lower threshold but the imbalance issue remains severe. Our BMC mechanism (c) predicts a per-pixel objectness map and any anchor within the BM with a value larger than a threshold can be a positive anchor. Thus, the positive vs. negative anchor imbalance issue can be effectively relieved.

from natural images. These ULD approaches adapt the Mask-RCNN [26] framework by constructing a pseudo segmentation mask for lesion regions as the extra supervision [1, 2, 5, 8, 9, 13] or extract more 3D context information from multi CT slice [3, 4, 6–10, 12] to assist the ULD training.

Most of the above approaches proposed [2, 4–9, 12, 13] for ULD are designed based on a two-stage, anchor-based detection framework, i.e., proposal generation followed by classification and regression as in Faster R-CNN [27]. While achieving good success, such a framework has inherent limitations: (i) *Anchor imbalance in stage-1* [28]. In the first stage, anchor-based methods first find out the positive (lesion) anchors and use them as the region of interest (RoI) proposals according to the IoU between anchors and ground-truth (GT) BBoxes. An anchor is considered positive if its IoU with any GT BBox is greater than the IoU threshold and negative otherwise. This idea helps natural images to get enough positive anchors because they may have a lot of GT BBoxes per image [28], but it isn't suitable for ULD. Most CT slices only have one or two GT lesion BBox(s), so the amount of positive anchors of lesions is rather limited. This limitation can cause severe RoI imbalance (our empirical statistics show the positive vs. negative proposal imbalance can be as large as 1:200 which is showed in Suppl. Material), thereby leading to difficulty in network convergence. (ii) *Insufficient supervision in stage-2*. In the second stage, each RoI proposal from the first stage gets a classification score indicating its probability of lesion vs. non-lesion. The RoI proposals with high classification scores are chosen to obtain the final lesion BBox predictions. Since various lesions may have similar appearances with the

other tissues; the RoI proposals from non-lesion regions can also get very high lesion classification scores. Hence, a single classification score cannot provide sufficient supervision information to remove the false detections in the second stage.

To tackle the above two challenges, recently Li et al. [11] propose a bounding map (BM) based two-stage ULD method, which uses a lower IoU threshold to determine anchor categories based on IoU mechanism, and uses the value of BM as the soft labels. In addition, the BMs are also used as pseudo lesion masks for a newly introduced segmentation branch in stage-2. However, such an approach still suffers from several issues: (i) generating BMs from BBox in a fixed manner without considering lesion size and shape differences leads to sub-optimum BM representation for small lesions; and (ii) using IoU to determine anchor categories may lead to incorrect classification for lesions with irregular shapes.

To address the above issues, while exploiting the advantages of the BM-based two-stage ULD method, we propose a novel training mechanism for ULD to effectively reduce positive vs. negative anchor imbalance via a BM-based conditioning (BMC) mechanism in stage-1 and improve lesion localization accuracy by leveraging a size-adaptive BM (ABM) for supervising the segmentation branch in stage-2. Different from the traditional IoU-based positive and negative anchors selection mechanism, we use two independent anchor classification and regression tasks by directly predicting a **per-pixel objectness map** and selecting positive anchors for regression based on *BM*s [11]. Specifically as shown in Fig. 1, we use the  $BM_{xy}$  [11] as objectness GT map and select anchors whose value is greater than a threshold  $B$  in  $BM_{xy}$  to the region proposal network (RPN) for pixel-wise objectness map regression. We further randomly mask out some background pixels in  $BM_{xy}$  during objectness training to keep the number of background pixels no more than two times of the foreground pixel number. In addition, we extend BM into size-adaptive BMs (ABMs) to handle diverse lesions, in which the small lesions will be enhanced to compensate its limited pixel number while the big lesions are weakened. We use an ABM-supervised segmentation branch in stage-2 to improve the lesion localization accuracy.

Our method works perfectly with two-stage ULD methods, so it can be integrated with the state-of-the-art (SOTA) two-stage ULD methods. We conduct extensive experiments on the DeepLesion dataset [29] with three SOTA ULD methods to validate the effectiveness of our method.

## 2 Method

As shown in Fig. 2, we utilize the BMC mechanism ((a) & (b) in Fig. 2) to reduce positive vs. negative anchor imbalance in stage-1 and improve lesion localization accuracy by adding a supervised segmentation branch based on size-adaptive BM (ABM) ((c) in Fig. 2) in stage-2. Section 2.1 details the BM generation process [11]; Section 2.2 introduces the BMC mechanism, and Section 2.3 explains the newly introduced ABM-supervised segmentation branch.

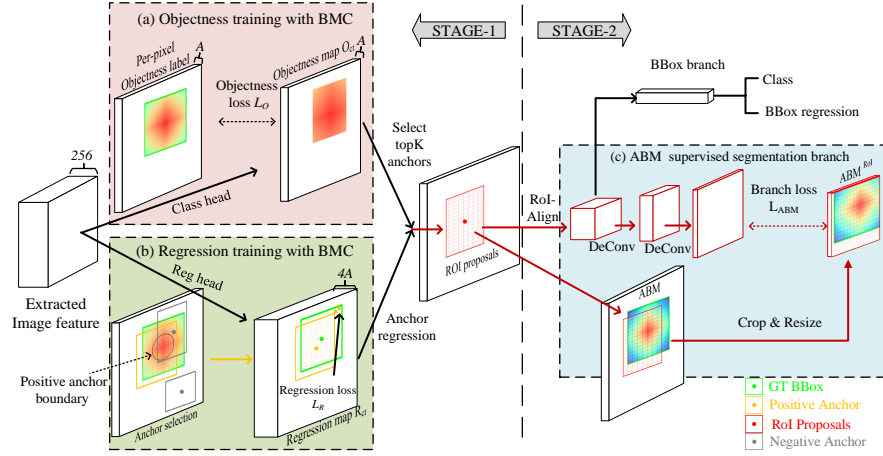


**Fig. 2.** The network architecture of the proposed approach, in which, BMC mechanism (a&b) and ABM branch (c) are respectively used in the two stages of the ULD method.

## 2.1 Bounding map generation

For the  $n^{\text{th}}$  GT BBox in an image  $I_{ct}$ , the BMs  $BM_x^{(n)}$  and  $BM_y^{(n)}$  are computed based on an all-zero map, in which the element values within the BBox at the same location as the GT BBox are assigned to values linearly interpolated from 1 to 0.5. The all-zero map and the final BMs have the same size as the image feature map output by the backbone network. Specifically,

$$BM_x^{(n)}(x, y) = \begin{cases} 0 & (x, y) \notin S_{BBox}^{(n)} \\ 1 - k_x^{(n)} |x^{(n)} - x_{ctr}^{(n)}| & (x, y) \in S_{BBox}^{(n)} \end{cases}, \quad (1)$$

$$BM_y^{(n)}(x, y) = \begin{cases} 0 & (x, y) \notin S_{BBox}^{(n)} \\ 1 - k_y^{(n)} |y^{(n)} - y_{ctr}^{(n)}| & (x, y) \in S_{BBox}^{(n)} \end{cases}, \quad (2)$$

where  $S_{BBox}^{(n)}$  denotes the  $n^{\text{th}}$  GT BBox  $(x_1^{(n)}, y_1^{(n)}, x_2^{(n)}, y_2^{(n)})$ , whose center is at  $(x_{ctr}^{(n)}, y_{ctr}^{(n)})$ . The slope  $k^{(n)}$  calculation is defined as:

$$k_x^{(n)} = \frac{1}{x_2^{(n)} - x_1^{(n)}}, \quad k_y^{(n)} = \frac{1}{y_2^{(n)} - y_1^{(n)}}, \quad (3)$$

and the final  $BM_x$  ( $BM_y$ ) is generated by aggregating all the  $BM_x^{(n)}$  s ( $BM_y^{(n)}$  s):

$$BM_x = \min \left[ \sum_{i=1}^I BM_x^{(n)}, 1 \right], \quad BM_y = \min \left[ \sum_{i=1}^I BM_y^{(n)}, 1 \right], \quad (4)$$

where  $N$  is the number of GT BBoxes of a CT image. Finally, the  $BM_{xy}$  is formed by element-wise multiplication between  $BM_x$  and  $BM_y$  [11]:

$$BM_{xy} = \sqrt[2]{BM_x \odot BM_y}, \quad (5)$$

Different from [11], we use only  $BM_{xy}$  and we will call it  $BM$  below.

## 2.2 BM-based conditioning mechanism

The RPN is trained to produce object bounding map  $R_{ct} \in \mathcal{R}^{\frac{W}{R} \times \frac{H}{R} \times 4A}$  via regression and objectness score map  $O_{ct} \in \mathcal{R}^{\frac{W}{R} \times \frac{H}{R} \times A}$  via classification at each position (or an anchor’s centerpoint) in an input image  $I_{ct} \in \mathcal{R}^{W \times H}$ , where  $R$  and  $A$  are the network output stride and the number of anchor classes, respectively. In previous ULDs, anchors are selected for training objectness and regression in conventional RPN; here we develop two independent BM-based processes for RoI proposal: (i) objectness map prediction with BMC and (ii) BBox regression with BMC.

**Objectness map prediction with BMC.** Conventionally, the objectness GT labels of positive, negative and otherwise anchors are set as 1, 0, and -1, respectively, and only the positive and negative anchors are used for loss calculation. Motivated by FCOS [30], we first resize  $BM \in \mathcal{R}^{W \times H \times A}$  into  $BM^r \in \mathcal{R}^{\frac{W}{R} \times \frac{H}{R} \times A}$  in a linear interpolation manner, then directly use  $BM^r$  as the objectness GT label and train RPN to predict the objectness map in a per-pixel manner as showed in Fig. 2 (a). Considering the lesion sizes variation and foreground-background pixel imbalance, we further randomly ignore some background pixels in  $BM^r$  to keep the number of background pixels no more than two times of the foreground pixel number  $N_f$ . Specifically, we first find out the foreground and background pixels set  $S_f$  and  $S_b$  based on  $BM^r$ :

$$S_f = \{(x_f, y_f) | BM_{xy}^r(x_f, y_f) \geq 0.5\}, S_b = \{(x_b, y_b) | BM_{xy}^r(x_b, y_b) < 0.5\}. \quad (6)$$

Then the number of foreground pixels  $N_f = Card(S_f)$  can be counted. After that, we randomly sample  $2N_f$  background pixels from the background pixels set  $S_b$  as the training set  $S_b^t$ . Finally, we train the RPN for predicting objectness map  $O_{ct} \in \mathcal{R}^{\frac{W}{R} \times \frac{H}{R} \times A}$  with a binary cross entropy (BCE) loss:

$$\mathcal{L}_o = \sum_{j=1}^J \mathcal{L}_{BCE}(O_{ct}(x_j, y_j), BM_{xy}^r(x_j, y_j)) \quad (x_j, y_j) \in S_b^t \cup S_f, \quad (7)$$

where  $J$  is the total number of pixels in  $S_b^t \cup S_f$ .

**BBox regression with BMC.** In our method, the loss computation during BBox regression is still applied to positive anchors, but we propose for BBox regression a new positive anchor selection method based on BM (see Fig. 2 (b)). We first define a positive anchor boundary value  $B$  and set the anchors whose corresponding  $BM_{xy}^r$  value is greater than  $B$  as positive anchors:

$$Loc_p^{(n)} = \begin{cases} \{x_p^{(n)}, y_p^{(n)} | BM_{xy}^{r(i)}(x_p^{(n)}, y_p^{(n)}) \geq B\} & A_{BBox}^{(n)} \geq 16 \\ \{x_p^{(n)}, y_p^{(n)} | BM_{xy}^{r(i)}(x_p^{(n)}, y_p^{(n)}) \geq 0.5\} & else \end{cases}, \quad (8)$$

where  $Loc_p^{(n)}$  and  $A_{BBox}^{(n)}$  is the positive anchor’s centerpoint location set for the  $n^{th}$  GT BBox and the area of the  $n^{th}$  GT BBox. Finally, we union all  $Loc_p^{(n)}$  and get  $Loc_p$ , the anchor centerpoint location set for the image.

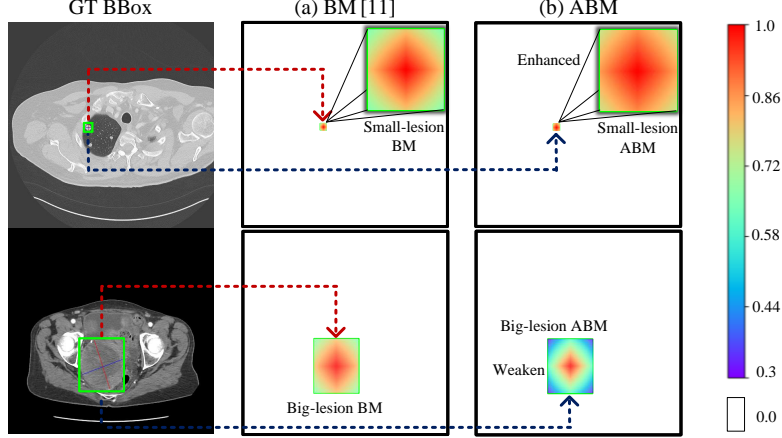


**Fig. 3.** Different from the BM (a) that uses a fixed generation method [11], the proposed ABM (b) can enhance the small lesions while weaken the big lesions.

Finally the BBox regression loss can be written as:

$$\mathcal{L}_r = \sum_{m=1}^M \mathcal{L}_{reg}(x_m, y_m) \quad (x_m, y_m) \in Loc_p, \quad (9)$$

where  $\mathcal{L}_{reg}$  is the original regression loss function and  $M$  is the number of anchors' centerpoint locations in  $Loc_p$ .

### 2.3 Pseudo lesion segmentation via ABM supervision.

The top-K objectness anchors regressed by the regression are used as RoI proposals and the input of the second-stage classification and regression. However, as we analyzed in Sec. 1, the BBox branch does not provide enough supervision for the complex ULD task. We introduce an extra branch, i.e., ABM supervised pseudo lesion segmentation branch.

**Size adaptive bounding maps (ABM).** As shown in Section 2.1, BM uses a fixed generating manner without considering lesion size and shape differences leads to sub-optimum representations for small lesions. As shown in Fig. 3, we extend BM to make it adaptive to lesion size, so that a small lesion is enhanced to compensate its limited area. Specifically, we multiply the two slopes  $k_x^{(n)}$  and  $k_y^{(n)}$  by a ratio  $\alpha$  when generating the  $ABM_x^{(n)}$  and  $ABM_y^{(n)}$ :

$$ABM_x^{(n)}(x, y) = \begin{cases} 0 & (x, y) \notin S_{BBox}^{(n)} \\ 1 - \alpha k_x^{(n)} |x^{(n)} - x_{ctr}^{(n)}| & (x, y) \in S_{BBox}^{(n)} \end{cases}, \quad (10)$$

$$ABM_y^{(n)}(x, y) = \begin{cases} 0 & (x, y) \notin S_{BBox}^{(n)} \\ 1 - \alpha k_y^{(n)} |y^{(n)} - y_{ctr}^{(n)}| & (x, y) \in S_{BBox}^{(n)} \end{cases}, \quad (11)$$

$$\alpha = \begin{cases} 0 & A_{BBox}^{(n)} < A_s \\ 1 & A_s \leq A_{BBox}^{(n)} < A_m \\ 1.4 & A_{BBox}^{(n)} \geq A_m \end{cases}, \quad (12)$$

where the  $A_s, A_m$  are the size thresholds for small and medium lesions. The final  $ABM_{xy}$  generation is the same as the  $BM_{xy}$ .

**Segmentation with ABM supervision.** As shown in Fig. 2 (c), the ABM supervised segmentation branch is the same as the mask branch in Mask R-CNN [26]. It is parallel to the BBox classification and regression branch. The ABM is first cropped based on the RoI BBox and resized to the size of the output to obtain  $ABM_x^{RoI} \in \mathcal{R}^{W_b \times H_b \times 1}$ , where  $W_b$  and  $H_b$  are the output  $\hat{ABM}^{RoI}$ 's width and height of ABM-supervised segmentation branch, respectively. Then the loss function of ABM branch for each RoI can be defined as a norm-2 loss:

$$\mathcal{L}_{ABM} = \mathcal{L}_2(\hat{ABM}^{RoI}, ABM^{RoI}). \quad (13)$$

## 3 Experiments

### 3.1 Dataset and setting

We conduct experiments on the DeepLesion dataset [29]. The dataset contains 32,735 lesions on 32,120 axial slices from 10,594 CT studies of 4,427 unique patients. Most existing datasets typically focus on one type of lesion, while DeepLesion contains a variety of lesions with large diameters ranges (from 0.21 to 342.5mm). The 12-bit intensity CT is rescaled to [0,255] with different window ranges settings used in different frameworks. Also, every CT slice is resized and interpolated according to the detection frameworks' setting. We follow the official split, i.e., 70% for training, 15% for validation and 15% for testing. The number of false positives per image (FPPI) is used as the evaluation metric. We set the positive anchor boundary value  $B$  in Equ. 8 as 0.25, size thresholds  $S_s$  and  $S_m$  in Equ. 12 as 250 and 1000 respectively. For training, we use the original network architecture and settings, and initialize the network using pretrained ULD models on DeepLesion dataset [29].

### 3.2 Lesion detection performance

We apply our method with four SOTA ULD approaches [6–9] to evaluate the effectiveness. We also compare with three SOTA anchor-free [30–32] and one two-stage anchor-based [27] detection methods. As shown in Table 1, our method brings promising detection performance improvements for all baselines. The improvements of Faster R-CNN [27], 9-slice 3DCE, and MVP-Net are more pronounced than those of MULAN w/o SRL [8] and AlignShift [9]. This is because MULAN and AlignShift introduce extra weakly segmentation mask generated from radiologist-annotated RECIST labels. The anchor-free methods get unsatisfactory results mainly because they are lack of the initialize advantage of anchors and the coarse-to-fine training advantage of the two-stage mechanism. We also provide a case to show our method's effectiveness in Suppl. Material.

**Table 1.** Sensitivity (%) at various FPPI on the testing set of DeepLesion [29].

Methods	slices	@0.5	@1	@2	@4	Avg.[0.5,1,2,4]
Faster R-CNN [27]	3	57.17	68.82	74.97	82.43	70.85
Faster R-CNN+BM [11]	3	63.96 (6.79↑)	74.43 (5.61↑)	79.80 (4.83↑)	86.28 (3.85↑)	76.12(5.27↑)
Faster R-CNN+Ours	3	<b>65.37 (8.20↑)</b>	<b>76.31 (7.49↑)</b>	<b>81.03 (6.06↑)</b>	<b>87.98 (5.55↑)</b>	<b>77.67(6.82↑)</b>
3DCE [6]	9	59.32	70.68	79.09	84.34	73.36
3DCE+BM [11]	9	64.38 (5.06↑)	75.55 (4.87↑)	82.74 (3.65↑)	87.78 (3.44↑)	77.62(4.26↑)
3DCE+Ours	9	66.98 (7.66↑)	77.25 (6.57↑)	83.64 (4.55↑)	88.41 (4.07↑)	79.07(5.71↑)
MVP-Net [7]	9	70.07	78.77	84.91	87.33	80.27
MVP-Net+BM [11]	9	72.12 (2.05↑)	80.51 (1.74↑)	86.08 (1.17↑)	88.41 (1.08↑)	81.78(1.51↑)
MVP-Net+Ours	9	73.05 (2.98↑)	81.41 (2.64↑)	87.22 (2.31↑)	89.37 (2.04↑)	82.76(2.49↑)
MULAN w/o (SRL&RECIST) [8]	9	72.34	80.17	85.21	89.41	81.78
MULAN w/o (SRL&RECIST) +BM [11]	9	74.71 (2.37↑)	81.62 (1.45↑)	86.44 (1.23↑)	89.82 (0.41↑)	83.15(1.37↑)
MULAN w/o (SRL&RECIST) +Ours	9	75.97 (3.63↑)	82.81 (2.64↑)	86.85 (1.64↑)	90.00(0.59↑)	83.91(2.13↑)
MULAN w/o SRL [8]	9	73.85	81.02	85.98	90.01	82.71
MULAN w/o SRL +Ours	9	76.28 (2.43↑)	83.13 (2.11↑)	87.30 (1.32↑)	90.49 (0.48↑)	84.30(1.59↑)
AlignShift w/o RECIST [9]	7	76.31	84.07	88.08	91.62	85.02
AlignShift w/o RECIST+BM [11]	7	77.51 (1.20↑)	84.95 (0.88↑)	88.63 (0.55↑)	92.08 (0.46↑)	85.79(0.77↑)
AlignShift w/o RECIST+Ours	7	79.03 (2.72↑)	85.63 (1.56↑)	89.53 (1.45↑)	92.43 (0.81↑)	86.66(1.64↑)
AlignShift [9]	7	77.20	84.38	89.03	92.31	85.73
AlignShift +Ours	7	<b>79.17 (1.97↑)</b>	<b>85.71 (1.33↑)</b>	<b>89.80 (0.77↑)</b>	<b>92.65 (0.34↑)</b>	<b>86.83(1.10↑)</b>
FCOS (anchor-free) [31]	3	37.78	54.84	64.12	77.84	58.65
Objects as points (anchor-free) [30]	3	34.87	43.58	52.41	64.01	48.72
Deformable detr (anchor-free) [32]	3	57.62	65.64	70.65	75.58	67.37

**Table 2.** Ablation study of our method at various FPs per image (FPPI).

AlignShift [9]	RECIST label	BMC objectness training	BMC regression training	ABM branch	BM branch [11]	FPPI=0.5	FPPI=1	Inference (s/img)
✓	✓					77.20	84.38	0.1758
✓	✓	✓				78.99	85.65	0.1747
✓	✓	✓	✓			<b>79.17</b>	<b>85.71</b>	0.1833
✓		✓	✓			77.95	84.99	0.1784
✓		✓	✓	✓		<b>79.03</b>	<b>85.63</b>	0.1814
✓		✓	✓		✓	77.97	85.04	0.1755

### 3.3 Ablation study

Ablation study is provided to evaluate the importance of the three key components of the proposed method: (i) Objectness map prediction with BMC, (ii) Box regression with BMC, and (iii) *ABM* supervised segmentation. As shown in Table 2, using objectness map prediction with BMC, we obtain a 1.79% improvement over the baseline. Further adding BBox regression training with BMC accounts for another 0.18% improvement and gives the best performance. Without using extra RECIST label, *ABM* and *BM* increases the performance by 1.08% and 0.02%, respectively. In addition, the use of our method brings a minor increase (less than 10%) in the inference time on a Titan RTX GPU.

## 4 Conclusion

In this paper, we try to overcome the two intrinsic limitations of two-stage ULD methods: anchor imbalance in stage-1 and insufficient supervision in stage-2. To relieve these, we propose a new BMC mechanism in stage-1 and an *ABM* supervised segmentation branch in stage-2. Extensive experiments using several SOTA baselines on the DeepLesion dataset show that our approach can effectively boost the ULD performance with almost no additional computational cost.



## References

1. M. Zlocha, Q. Dou, and B. Glocker. Improving retinanet for ct lesion detection with dense masks from weak recist labels. In *MICCAI*, pages 402–410. Springer, 2019.
2. Q. Tao, Z. Ge, J. Cai, J. Yin, and S. See. Improving deep lesion detection using 3d contextual and spatial attention. In *MICCAI*, pages 185–193. Springer, 2019.
3. N. Zhang, D. Wang, X. Sun, P. Zhang, C. Zhang, Y. Cao, and B. Liu. 3d anchor-free lesion detector on computed tomography scans. *arXiv:1908.11324*, 2019.
4. N. Zhang, Y. Cao, B. Liu, and Y. Luo. 3d aggregated faster R-CNN for general lesion detection. *arXiv:2001.11071*, 2020.
5. Y. Tang, K. Yan, Y. Tang, J. Liu, J. Xiao, and R. M Summers. Uldor: a universal lesion detector for ct scans with pseudo masks and hard negative example mining. In *IEEE ISBI*, pages 833–836, 2019.
6. K. Yan, M. Bagheri, and R. M Summers. 3d context enhanced region-based convolutional neural network for end-to-end lesion detection. In *MICCAI*, pages 511–519. Springer, 2018.
7. Z. Li, S. Zhang, J. Zhang, K. Huang, Y. Wang, and Y. Yu. Mvp-net: Multi-view fpn with position-aware attention for deep universal lesion detection. In *MICCAI*, pages 13–21. Springer, 2019.
8. K. Yan, Y. Tang, Y. Peng, V. Sandfort, M. Bagheri, Z. Lu, and R. M Summers. Mulan: Multitask universal lesion analysis network for joint lesion detection, tagging, and segmentation. In *MICCAI*, pages 194–202. Springer, 2019.
9. Jiancheng Yang, Yi He, Xiaoyang Huang, Jingwei Xu, Xiaodan Ye, Guangyu Tao, and Bingbing Ni. Alignshift: bridging the gap of imaging thickness in 3d anisotropic volumes. In *MICCAI*, pages 562–572. Springer, 2020.
10. Jinzheng Cai, Ke Yan, Chi-Tung Cheng, Jing Xiao, Chien-Hung Liao, Le Lu, and Adam P Harrison. Deep volumetric universal lesion detection using light-weight pseudo 3d convolution and surface point regression. In *MICCAI*, pages 3–13. Springer, 2020.
11. Han Li, Hu Han, and S Kevin Zhou. Bounding maps for universal lesion detection. In *MICCAI*, pages 417–428. Springer, 2020.
12. Shu Zhang, Jincheng Xu, Yu-Chun Chen, Jiechao Ma, Zihao Li, Yizhou Wang, and Yizhou Yu. Revisiting 3d context modeling with supervised pre-training for universal lesion detection in ct slices. In *MICCAI*, pages 542–551. Springer, 2020.
13. Ke Yan, Jinzheng Cai, Youjing Zheng, Adam P Harrison, Dakai Jin, You-bao Tang, Yu-Xing Tang, Lingyun Huang, Jing Xiao, and Le Lu. Learning from multiple datasets with heterogeneous and partial labels for universal lesion detection in ct. *IEEE Trans. Med. Imag.*, 2020.
14. F. Liao, M. Liang, Z. Li, X. Hu, and S. Song. Evaluate the malignancy of pulmonary nodules using the 3-d deep leaky noisy-or network. *IEEE Trans. Neural Netw. Learn. Syst.*, 30(11):3484–3495, 2019.
15. Y. Lin, J. Su, X. Wang, X. Li, J. Liu, K. Cheng, and X. Yang. Automated pulmonary embolism detection from ctpa images using an end-to-end convolutional neural network. In *MICCAI*, pages 280–288. Springer, 2019.
16. X. Wang, S. Han, Y. Chen, D. Gao, and N. Vasconcelos. Volumetric attention for 3d medical image segmentation and detection. In *MICCAI*, pages 175–184. Springer, 2019.
17. M. Astaraki, I. Toma-Dasu, Ö. Smedby, and C. Wang. Normal appearance auto-encoder for lung cancer detection and segmentation. In *MICCAI*, pages 249–256. Springer, 2019.

18. C. Tang, H. and Zhang and X. Xie. NoduleNet: Decoupled false positive reduction for pulmonary nodule detection and segmentation. In *MICCAI*, pages 266–274. Springer, 2019.
19. Q. Shao, L. Gong, K. Ma, H. Liu, and Y. Zheng. Attentive ct lesion detection using deep pyramid inference with multi-scale booster. In *MICCAI*, pages 301–309. Springer, 2019.
20. J. Liu, L. Cao, O. Akin, and Y. Tian. 3dfpn-hs: 3d feature pyramid network based high sensitivity and specificity pulmonary nodule detection. In *MICCAI*, pages 513–521. Springer, 2019.
21. Thomas Boot and Humayun Irshad. Diagnostic assessment of deep learning algorithms for detection and segmentation of lesion in mammographic images. In *MICCAI*, pages 56–65. Springer, 2020.
22. Xin Yu, Bin Lou, Donghao Zhang, David Winkel, Nacim Arrahmane, Mamadou Diallo, Tongbai Meng, Heinrich von Busch, Robert Grimm, Berthold Kiefer, et al. Deep attentive panoptic model for prostate cancer detection using biparametric mri scans. In *MICCAI*, pages 594–604. Springer, 2020.
23. Dongyi Fan, Chengfen Zhang, Bin Lv, Lilong Wang, Guanzheng Wang, Min Wang, Chuanfeng Lv, and Guotong Xie. Positive-aware lesion detection network with cross-scale feature pyramid for oct images. In *MICCAI*, pages 685–693. Springer, 2020.
24. Junxiong Yu, Chaoyu Chen, Xin Yang, Yi Wang, Dan Yan, Jianxing Zhang, and Dong Ni. Computer-aided tumor diagnosis in automated breast ultrasound using 3d detection network. In *MICCAI*, pages 181–189. Springer, 2020.
25. Maria V Sainz de Cea, Karl Diedrich, Ran Bakalo, Lior Ness, and David Richmond. Multi-task learning for detection and classification of cancer in screening mammography. In *MICCAI*, pages 241–250. Springer, 2020.
26. K. He, G. Gkioxari, P. Dollár, and R. Girshick. MASK R-CNN. In *IEEE ICCV*, pages 2961–2969, 2017.
27. S. Ren, K. He, R. Girshick, and J. Sun. Faster R-CNN: Towards real-time object detection with region proposal networks. In *NIPS*, pages 91–99, 2015.
28. K. Oksuz, B. C. Cam, S. Kalkan, and E. Akbas. Imbalance problems in object detection: A review. *Trans. Pattern Anal. Mach. Intell.*, 2020.
29. K. Yan, X. Wang, L. Lu, L. Zhang, A. P Harrison, M. Bagheri, and R. M Summers. Deep lesion graphs in the wild: relationship learning and organization of significant radiology image findings in a diverse large-scale lesion database. In *IEEE CVPR*, pages 9261–9270, 2018.
30. X. Zhou, D. Wang, and P. Krähenbühl. Objects as points. *arXiv:1904.07850*, 2019.
31. Z. Tian, C. Shen, H. Chen, and T. He. Fcos: Fully convolutional one-stage object detection. In *IEEE ICCV*, pages 9627–9636, 2019.
32. Xizhou Zhu, Weijie Su, Lewei Lu, Bin Li, Xiaogang Wang, and Jifeng Dai. Deformable detr: Deformable transformers for end-to-end object detection. *arXiv preprint arXiv:2010.04159*, 2020.

# Supplementary Materials for Conditional Training with Bounding Map for Universal Lesion Detection

Paper ID 487

Anonymous Organization

## 1 Visualization of detection results

We randomly choose four CT images from DeepLesion dataset [1] to visually compare the detection results of AlignShift [2] w/ and w/o our methods. As shown in Fig. 1, the number of high-classification-score FP predictions is decreased (a&c&d) and more accurate results (b) are obtained with the help of our method.

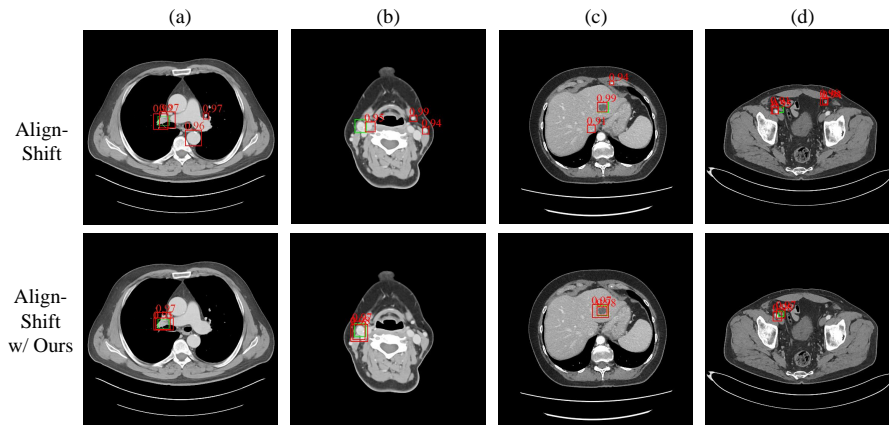


**Fig. 1.** High score BBoxes prediction (above 0.9) of AlignShift [2] with or without proposed method on test images. Red and green BBoxes denotes predicted BBoxes and GT BBoxes, respectively. The scores are marked above the BBoxes.

## 2 The number of positive anchors based on IoU

We compute the number of matched positive anchors per image (a in Fig. 2) and per GT BBoxes (b in Fig. 2) based on the IoU mechanism. The IoU threshold is set as 0.7. As shown in Fig. 2, the number of positive anchors is very few

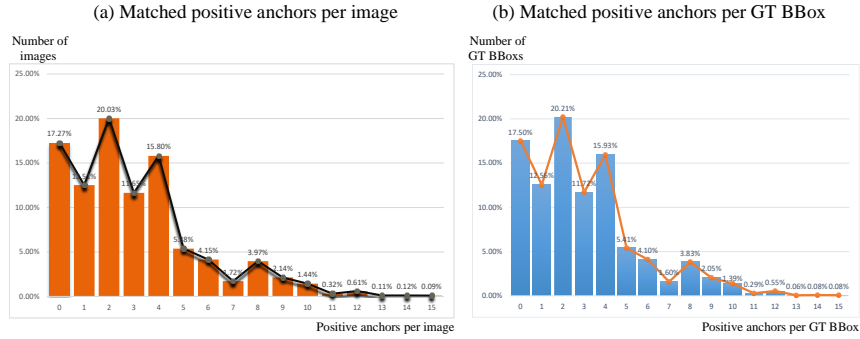


**Fig. 2.** We count the number of matched positive anchors per image (a) and per GT BBoxes (b) based on the IoU mechanism.

for both per-image manner and per-GT-BBox manner. More than 70% of GT-BBoxes (or images) match no greater than four positive anchors. This will cause a high imbalance of positive anchors v.s. negative anchors during training.

## References

1. K. Yan, X. Wang, L. Lu, L. Zhang, A. P Harrison, M. Bagheri, and R. M Summers. Deep lesion graphs in the wild: relationship learning and organization of significant radiology image findings in a diverse large-scale lesion database. In *IEEE CVPR*, pages 9261–9270, 2018.
2. Jiancheng Yang, Yi He, Xiaoyang Huang, Jingwei Xu, Xiaodan Ye, Guangyu Tao, and Bingbing Ni. Alignshift: bridging the gap of imaging thickness in 3d anisotropic volumes. In *MICCAI*, pages 562–572. Springer, 2020.